

Probing the Electron States and Metal-Insulator Transition Mechanisms in Atomically Thin MoS₂ Based on Vertical Heterostructures

Xiaolong Chen¹, Zefei Wu¹, Shuigang Xu¹, Lin Wang², Rui Huang^{1,3}, Yu Han¹, Weiguang Ye¹,
Wei Xiong¹, Tianyi Han¹, Gen Long¹, Yang Wang¹, Yuheng He¹, Yuan Cai¹, Ping Sheng¹, Ning
Wang^{1*}

¹*Department of Physics and the William Mong Institute of Nano Science and Technology, the
Hong Kong University of Science and Technology, Clear Water Bay, Hong Kong, China*

²*Department of Condensed Matter Physics, Group of Applied Physics, University of Geneva, 24
Quai Ernest Ansermet, CH1211 Geneva, Switzerland*

³*Department of Physics and Electronic Engineering, Hanshan Normal University, Chaozhou,
Guangdong, 521041, China*

*Correspondence should be addressed to: Ning Wang, phwang@ust.hk

The metal-insulator transition (MIT) is one of the remarkable electrical transport properties of atomically thin molybdenum disulphide (MoS₂). Although the theory of electron-electron interactions has been used in modeling the MIT phenomena in MoS₂, the

underlying mechanism and detailed MIT process still remain largely unexplored. Here, we demonstrate that the vertical metal-insulator-semiconductor (MIS) heterostructures built from atomically thin MoS₂ (monolayers and multilayers) are ideal capacitor structures for probing the electron states in MoS₂. The vertical configuration of MIS heterostructures offers the added advantage of eliminating the influence of large impedance at the band tails and allows the observation of fully excited electron states near the surface of MoS₂ over a wide excitation frequency (100 Hz-1 MHz) and temperature range (2 K- 300 K). By combining capacitance and transport measurements, we have observed a percolation-type MIT, driven by density inhomogeneities of electron states, in the vertical heterostructures built from monolayer and multilayer MoS₂. In addition, the valence band of thin MoS₂ layers and their intrinsic properties such as thickness-dependence screening abilities and band gap widths can be easily accessed and precisely determined through the vertical heterostructures.

Molybdenum disulphide (MoS₂), a n-type semiconductor¹⁻¹⁶, shows novel properties such as superconductivity⁶, controllable valley polarization^{17, 18} and metal-insulator transition³⁻⁶ (MIT). In MoS₂ field-effect transistors (FETs), gate-induced charge carriers transport in a thin layer near the surface of MoS₂ and are vulnerable to charge impurities and different types of disorder^{2, 3, 12, 14, 19, 20}. The presence of a high-k dielectric material³ to monolayer MoS₂ can effectively screen charge impurities and allow the observation of MIT. Based on recent transport measurements³, the phase transition behavior of monolayer MoS₂ has been attributed to transition from an insulating phase, in which disorder suppresses the electronic interactions, to a metallic phase in which strong coulomb interactions occur. However, the underlying physical mechanism and detailed MIT process need to be further clarified. Different from the studies on transport

properties of MoS₂, the capacitance spectroscopy¹⁴ recently applied to the characterization of MoS₂ FET structures has been demonstrated as one of the most convenient and powerful method for studying the electron states in MoS₂ at room temperature. At low temperatures, however, the information obtained by this technique is limited due to the large impedance near the band edge of MoS₂. Different from that in graphene quantum capacitors²¹⁻²⁷, the slow charge carrier mobility in MoS₂ capacitors often leads to incompletely charged states, mainly due to the localization near the band edge. The incompletely charged capacitance confuses the effect of charge traps.

Here, we show an approach to address these problems by introducing a MoS₂-based vertical metal-insulator-semiconductor-metal (MIS-M) heterostructure suitable for probing electron states using capacitance measurements. Unlike conventional FET structures¹⁴, our approach eliminates the impedance effects and can directly access the intrinsic characteristics of thin-layer MoS₂ over a wide frequency (100 Hz- 1 MHz) and temperature range (2 K-300 K). By combining capacitance and transport measurements, we show that the MIT observed in monolayer and multilayer MoS₂ is consistent with the physical picture of a percolation²⁸⁻³⁵ transition model. The results of our investigation on the mechanisms of MIT and other intrinsic characteristics, such as thickness-dependent screening abilities and fast relaxation of hole carriers at the valence band, provide useful information much needed for improving the performance of the FET devices based on MoS₂ monolayers and multilayers.

MoS₂ vertical heterostructural capacitance devices

Figs. 1a and 1b illustrate our specially designed MIS-M capacitor device, fabricated by transferring^{23, 36} exfoliated flakes of MoS₂ and hexagonal boron nitride (BN) on a Si substrate

coated with a SiO₂ thin layer (300 nm). Exfoliated natural crystals of monolayer or multilayer MoS₂ were first transferred onto a BN sheet, serving as an ultra-smooth and disorder-free gate dielectric³⁷. A Ti/Au (10 nm/20 nm) local gate sits underneath the BN sheet. The critical step in achieving MIS-M structure is to have the MoS₂ sheet fully covered by a top electrode (Ti/Au: 10 nm/50 nm). The equivalent circuit of this device geometry is shown in Fig. 1c. The measured capacitance C_t is the total capacitance contributed by two capacitors originating from the BN layer (C_{BN}) and MoS₂ (C_{MoS}) in serial connection, plus the residue capacitance C_p in parallel connection. C_t , shown below, is the capacitance wiping off C_p (see detailed analysis in Supplementary Material). Therefore, $C_t = (C_{MoS}^{-1} + C_{BN}^{-1})^{-1}$. With fully-covered top electrodes, carriers can respond vertically instead of moving in the plane of MoS₂. This unique structure directly avoids the huge lateral resistance R of MoS₂ near the band edge. As a result, the measured C_t (of a 5.9 nm-thick MoS₂) at 2 K (Fig. 1d) is almost independent of excitation frequencies f , which differs greatly from that obtained in conventional FET structure devices^{7, 14}. In capacitance measurement of conventional FET structures, lateral resistance R must be considered when $R \sim 1/(2\pi f C_t)$. This is confirmed by our MoS₂ capacitance devices with partially-covered top electrodes which show significant frequency-dependent and temperature-dependent characteristics (Supplementary Material). We also achieved good Ohmic contacts between the top Ti/Au electrode and MoS₂ in our devices, as evidenced by the capacitance measurements at different excitation voltages (Fig. 1e). Note that the capacitance measured at large excitation voltages (e.g. at 2V) shows deviation due to the averaging effect.

Characterization of the vertical MIS-M structures

The interface structure and band diagrams in the MoS₂-based MIS-M devices are shown schematically in Figs. 4a-d. When the gate voltage $V_g > 0$, electrons accumulate at the MoS₂ surface (Fig. 4b). The measured capacitance approaches $C_{\max} = C_{BN} = \frac{\epsilon_{BN}}{d_{BN}}$ when V_g is sufficiently large, where ϵ_{BN} and d_{BN} are the dielectric constant and the thickness of BN respectively, while under negative V_g (Fig. 4c) electrons are depleted. In this case, the measured capacitance can be described by $C_{\min} = \left(\frac{d_{BN}}{\epsilon_{BN}} + \frac{d_{MoS}}{\epsilon_{MoS}}\right)^{-1}$, where ϵ_{MoS} and d_{MoS} are the dielectric constant and the thickness of MoS₂ respectively. This allows us to directly obtain the $\epsilon_{MoS} - d_{MoS}$ relationship of MoS₂.

As shown in Fig. 2, ϵ_{MoS} has been found to increase from $3.9 \epsilon_0$ for a monolayer to $10.5 \epsilon_0$ for bulk MoS₂. This is in excellent agreement with theoretical predictions^{38, 39}. The small ϵ_{MoS} in monolayer MoS₂ suggests poor dielectric screening of Coulomb interactions, indicating that strong electron-electron interactions could be achieved in clean monolayer MoS₂. The largely increased mobility observed in monolayer MoS₂ placed in a high- κ dielectric environment^{2, 3, 40} probably benefits from its small ϵ_{MoS} . In fact, the decrease in the optical phonon mode E_{2g}^1 observed by a Raman spectroscopy study of few-layer and bulk MoS₂⁴¹ is also due to the strong dielectric screening effects.

The valence band of multilayer MoS₂ is also accessed by detecting the inversion layer of holes using low excitation frequencies at sufficiently high temperatures (Fig. 3a and b). However, the inversion layer is invisible when using high frequencies at low temperatures ($T < 100$ K). This is due to the presence of the Schottky-barrier between the Ti/Au contact and the valence band⁷.

Holes must form through thermal excitations or minute current leakage into the contacts. This process often requires a long time from ~ms to seconds. In the 12 nm-thick MoS₂ capacitance device, the majority of hole carriers have been relaxed around 20 kHz at 300 K, as confirmed by the phase information of the device, which is defined by $\Theta = \arctan(G/2\pi fC_iV)$, where G is the conductance and V is the excitation voltage. As shown in Fig. 3c, the phase peaks appear at about 20 kHz for different negative gate bias voltages, indicating that the relaxation time of holes in the 12 nm-thick MoS₂ device is around 50 μ s. For the capacitance samples contacted by Cr/Au top electrodes (Cr has a larger work function (~4.5 eV) than that of Ti (~4.3 eV)), a short relaxation time (~5 μ s) for holes has also been achieved at 300 K (Supplementary Material).

By applying the Poisson equation to model the vertical heterostructures in a quasi-quantitative manner (Supplementary Material), we correlated the quantum capacitance C_q of MoS₂ with the surface potential V_s in our capacitance devices. V_s is extracted based on the charge conservation relation $V_s = \int_0^{V_g} (1 - \frac{C_t}{C_{BN}}) dV_g$. The C_q - V_s relation is shown in Fig. 3d, yielding a band gap around 1.14 eV, which is close to the reported value of 1.2 eV⁴².

Percolation-induced MIT in monolayer and multilayer MoS₂

Similar to the MIT observed in transport measurements³⁻⁶, the capacitance data of the 5.9 nm-thick MoS₂ device measured at different temperatures (Fig. 4m) show an interesting transition with a well-defined cross-over point (at $V_g=5$ V and corresponding to a carrier density $n \sim 6.8 \times 10^{12} \text{ cm}^{-2}$, obtained from $n = C_{BN}(V_g - V_s - V_T)/e$, where $V_T \sim -1$ V is the threshold voltage). When $V_g < 5$ V, C_t decreases with decreasing temperature, whereas at $V_g > 5$ V the

temperature dependence of C_i is reversed. The observed cross-over point in capacitance measurements is indeed related to the MIT as its value ($\sim 6.8 \times 10^{12} \text{ cm}^{-2}$) is consistent with that measured by transport (Ref. 6 and Fig. 6). More evidence is provided by capacitance measurements of monolayer MoS₂ samples (Fig. 5a). In monolayer MoS₂, the intersections of the capacitance curves showed obvious temperature-dependent characteristics. At temperatures below 100 K, we observed that the cross-over point was stabilized roughly at $n \sim 1.2 \times 10^{13} \text{ cm}^{-2}$, consistent with the transport results measured in monolayer MoS₂³ with a MIT at $n \sim 1 \times 10^{13} \text{ cm}^{-2}$. Bilayer and trilayer MoS₂ samples displayed similar transition phenomena with cross-over points around $n \sim 8.6 \times 10^{12} \text{ cm}^{-2}$ (Fig. 5b).

The electronic transport of MoS₂ suffers from charge impurities^{2,3} and short-range disorders^{12, 14, 19, 20}, such as ripples, dislocation and sulphur vacancies. These disorders result in the insulating transport behaviour of MoS₂ in the low carrier density region, where electrons transport through hopping between localized states (Fig. 4j) and can be well described by the variable-range-hopping model^{3, 12, 20}. In the region where sufficient large carrier densities are introduced, metal behaviour is observed³. Here, we propose a percolation-type MIT in MoS₂, driven by density inhomogeneity of electron states²⁸⁻³⁵ which describes the systems in which charge carriers are transported through percolating conductive channels in the disorder landscapes due to the poor screening effect at low carrier densities. When carrier density is low enough, conductive paths are efficiently blocked and MIT occurs. MoS₂ has been proven to be such a disordered system, with impurity concentration ranging from 10^{11} cm^{-2} to 10^{13} cm^{-2} , especially for monolayer MoS₂, which is more vulnerable to ripples and charge impurities^{2, 3, 12, 14, 19, 20}. Thus, the MIT in MoS₂ is in line with the percolation transition theory in which disorder plays an important role. Moreover, our capacitance and transport data, shown below, provide further evidences to this effect.

The evolution of concentration and effective thickness of electron states probed by capacitance measurements can explain the observed MIT in transport measurements fairly well and provide details of the percolation transition process. The percolation transition phenomenon is illustrated in Fig. 4j-k. With increasing carrier densities n (by increasing gate voltage), the localized electron states begin to percolate with each other till a conductive channel occurs at a critical density (Fig. 4k). Further increasing carrier densities will lead to sufficient conductive channels spanning the entire system and result in metal-like transport behaviours (Fig. 4l). On the other hand, at the same carrier density, the effective thickness $d_{eff} = \frac{\epsilon_{MoS}}{C_{MoS}}$ of electron states confined in the surface of MoS₂ can be tuned by varying temperatures (Fig. 4n). Smaller d_{eff} can also be achieved at higher gate voltages where large amounts of surface charges are induced (supported by theoretical calculations in the Supplementary Material). As illustrated in Fig. 4e-i (assuming n remains unchanged), more conductive channels are formed at a smaller d_{eff} . The MIT should occur when d_{eff} is sufficiently small. The capacitance data of our samples (Fig. 4n and o) are similar to those obtained from transport measurements in multilayer MoS₂ (showing a MIT at $n=6.7 \times 10^{12} \text{ cm}^{-2}$)⁶. When $n < 6.8 \times 10^{12} \text{ cm}^{-2}$, d_{eff} decreases with increasing temperatures. Hence, the conductivity should increase as the temperature increases. In contrast, when $n > 6.8 \times 10^{12} \text{ cm}^{-2}$, the increase of d_{eff} would lead to decreasing conductivity as the temperature increases. Furthermore, the increasing n and decreasing d_{eff} would also enhance the screening of disorders and electron states and thus lead to increasing conductivity, while lowering the Coulomb interaction strength.

The percolation transition also suggests an increasing transition density at the cross-over point with increasing impurity concentration³⁰⁻³². In our MoS₂ samples the transition density was in the range 10¹²-10¹³cm⁻² due to the presence of large amounts of impurities. Moreover, the transition density in monolayer MoS₂ (~1×10¹³cm⁻²) was larger than that observed in multilayer MoS₂ (~6×10¹²cm⁻²), which agreed with the prediction of percolation theory as monolayer MoS₂ was more vulnerable to disorders. This was further evidenced by extracting charge trap densities, D_{it} , of MoS₂ from capacitance measurements (a trilayer sample shown in Fig. 5c). The presence of impurities or disorder may cause charge-trapping effects in MoS₂ capacitance devices, particularly at low temperatures. The charge traps can be fully excited only at relatively low frequencies (e.g. 100 Hz). The density of the charge traps can then be estimated by measuring the difference in capacitance at low and high frequencies, i.e., $D_{it} = (C_{MoS}(low_f) - C_{MoS}(high_f)) / e$. The trap densities in our monolayer and trilayer MoS₂ samples were in the order of 10¹²eV⁻¹cm⁻² (Fig. 5d). The trap densities in monolayer MoS₂ were apparently large, suggesting that monolayer MoS₂ is more sensitive to disorder. In fact, the trap densities in our samples were underestimated because of the limitation of the excitation frequency ranges. At relatively high temperatures (inset of Fig. 5c), the charge traps were easily excited, and the capacitances measured at low and high frequency show no difference.

At the transition point $n \sim 1.2 \times 10^{13} \text{cm}^{-2}$ in monolayer MoS₂, a large ratio $r_s = \frac{m^* e^2}{2\pi\epsilon_{MoS}\hbar^2\sqrt{\pi n}} \approx 7.1$ of Coulomb energy and kinetic energy was obtained, with measured $\epsilon_{MoS} = 3.9\epsilon_0$ and effective electron mass $m^* = 0.45m_0$ ^{3, 11}. However, in such strong interacting systems, negative compressibility was not observed by capacitance measurements. This is probably due to the suppression of Coulomb interactions by large amounts of impurities present

in MoS₂. Thus the density inhomogeneity induced by the impurities should still dominate the properties at the transition point.

The percolation induced MIT in MoS₂ is further supported by transport data at low temperatures. The MITs of multilayer (Fig. 6a) and monolayer (Fig. 6b) MoS₂ are clearly shown by the conductivity σ , at different temperatures, similar to previous reports³⁻⁶. The MIT occurs at $n \sim 6 \times 10^{12} \text{ cm}^{-2}$ for multilayer MoS₂ and $n \sim 1.1 \times 10^{12} \text{ cm}^{-2}$ for monolayer MoS₂, consistent with the capacitance data. To gain further insight into the transition behavior, we applied the percolation model of conductivity^{31, 32, 35} near the percolation threshold density n_c , which is described by

$$\sigma = A(n - n_c)^\delta$$

where A is a constant of proportionality and δ is the percolation exponent. Below the threshold density n_c , the 2D electron gas broke up into isolated puddles of carriers with no conducting channels crossing the whole sample. The conductivity showed insulating behavior and eventually vanished at $T = 0\text{K}$. In 2D systems, δ is expected to be $4/3$ ^{30, 31}. Based on the percolation model, we fit our experimental data of multilayer (Fig. 6c) and monolayer (Fig. 6d) MoS₂ samples at 2 K. The experimental results show excellent agreement with theoretical predictions. The extracted parameters are $\delta \sim 1.7$ and $n_c \sim 3.2 \times 10^{12} \text{ cm}^{-2}$ in multilayer MoS₂ and $\delta \sim 1.8$ and $n_c \sim 3.8 \times 10^{12} \text{ cm}^{-2}$ in monolayer MoS₂. The obtained percolation exponents are consistent with experimental values $\delta = 1.4-1.7$ found in other 2D systems, such as GaAs/AlGaAs heterostructures^{31, 32}. There was a slight deviation between experimental data and fitting curves at low carrier densities due to enhanced hopping conductivity and quantum tunneling at finite temperatures.

Conclusions

The vertical MIS heterostructures built from atomically thin MoS₂ are ideal capacitor structures for probing the electron states and intrinsic properties of MoS₂. Based on the analyses of experimental data obtained by electrical transport measurement and capacitance spectroscopy, we believe that the percolation-type MIT (driven by density inhomogeneities of electron states) is the dominating mechanism of the MIT in both monolayer and multilayer MoS₂. The vertical heterostructures offer the added advantages of eliminating the influence of large impedance at the band tails and accessing intrinsic characteristics such as thickness-dependence dielectric constant and band gap variation in atomically thin MoS₂. The present study also provides a new approach to characterizing the intrinsic properties of other atomically thin-layered materials and interface states of heterostructures built from 2D materials.

Methods

Sample preparation. Monolayer and multilayer MoS₂ flakes were exfoliated from molybdenum disulphide crystals (from 2D Semiconductors) by the micromechanical cleavage technique. MoS₂ and BN flakes were placed on the surface of a glass slide coated with PDMS/MMA as described for graphene-BN device fabrication³⁶. Then, these thin flakes were transferred onto a local Ti/Au (10nm/20nm) gate. The top electrodes were patterned using standard electron-beam lithography. Two types of top electrodes, Ti/Au (10nm/50nm) and Cr/Au (2nm/50nm), were fabricated through electron-beam evaporation. The dielectric constant of the BN sheet is measured by calibrating an internal reference capacitor that sits near the MoS₂ capacitance device (Fig. 1a). The thicknesses of MoS₂ and BN flakes were measured by an atomic force microscope (Veeco-Innova).

Capacitance and transport measurements. Capacitance measurements were carried out using an HP Precision 4284A LCR Meter with a sensitivity of ~ 0.1 fF in a cryogenic system (2 K- 300 K). All wires in the measurement circuits were shielded and the p-Si substrates were also grounded to minimize residual capacitance. The residual capacitance in the measurement setup is at the order of 1 fF (see Supplementary Material). Transport measurements were performed in the same cryogenic system using lock-in techniques.

Acknowledgements

The authors are grateful for fruitful discussions with Prof. Z. Q. Zhang from HKUST. Financial support from the Research Grants Council of Hong Kong (Project Nos. HKU9/CRF/13G, 604112, HKUST9/CRF/08 and N_HKUST613/12) and technical support of the Raith-HKUST Nanotechnology Laboratory for the electron-beam lithography facility at MCPF (Project No. SEG_HKUST08) are hereby acknowledged.

Author contributions

X. C. is the main contributor who initiated and conducted most experiments including sample fabrication, data collection and analyses. N. W. is the principle investigator and coordinator of this project. X. C., N. W., and P. S. provided the physical interpretation and wrote the manuscript. Other authors provided technical assistance in sample preparation, data collection/analyses and experimental setup.

Competing financial interests

The authors declare no competing financial interests.

References

1. Novoselov, K.S. et al. Two-dimensional atomic crystals. *Proc. Natl. Acad. Sci. USA* **102**, 10451-10453 (2005).
2. Radisavljevic, B., Radenovic, A., Brivio, J., Giacometti, V. & Kis, A. Single-layer MoS₂ transistors. *Nature Nanotech.* **6**, 147-150 (2011).
3. Radisavljevic, B. & Kis, A. Mobility engineering and a metal-insulator transition in monolayer MoS₂. *Nature Mater.* **12**, 815-820 (2013).
4. Baugher, B.W.H., Churchill, H.O.H., Yang, Y.F. & Jarillo-Herrero, P. Intrinsic electronic transport properties of high-quality monolayer and bilayer MoS₂. *Nano Lett.* **13**, 4212-4216 (2013).
5. Schmidt, H. et al. Transport properties of monolayer MoS₂ grown by chemical vapor deposition. *Nano Lett.* **14**, 1909-1913 (2014).
6. Ye, J.T. et al. Superconducting dome in a gate-tuned band insulator. *Science* **338**, 1193-1196 (2012).
7. Kim, S. et al. High-mobility and low-power thin-film transistors based on multilayer MoS₂ crystals. *Nature Commun.* **3**, 1011 (2012).
8. Lee, G.H. et al. Flexible and transparent MoS₂ field-effect transistors on hexagonal boron nitride-graphene heterostructures. *ACS Nano* **7**, 7931-7936 (2013).
9. Britnell, L. et al. Strong light-matter interactions in heterostructures of atomically thin films. *Science* **340**, 1311-1314 (2013).

10. Lopez-Sanchez, O., Lembke, D., Kayci, M., Radenovic, A. & Kis, A. Ultrasensitive photodetectors based on monolayer MoS₂. *Nature Nanotech.* **8**, 497-501 (2013).
11. Yoon, Y., Ganapathi, K. & Salahuddin, S. How good can monolayer MoS₂ transistors be? *Nano Lett.* **11**, 3768-3773 (2011).
12. Ghatak, S., Pal, A.N. & Ghosh, A. Nature of electronic states in atomically thin MoS₂ field-effect transistors. *ACS Nano* **5**, 7707-7712 (2011).
13. Wang, Q.H., Kalantar-Zadeh, K., Kis, A., Coleman, J.N. & Strano, M.S. Electronics and optoelectronics of two-dimensional transition metal dichalcogenides. *Nature Nanotech.* **7**, 699-712 (2012).
14. Zhu, W.J. et al. Electronic transport and device prospects of monolayer molybdenum disulphide grown by chemical vapour deposition. *Nature Commun.* **5**, 3087 (2014).
15. Liu, K.K. et al. Growth of large-area and highly crystalline MoS₂ thin layers on insulating substrates. *Nano Lett.* **12**, 1538-1544 (2012).
16. Zhan, Y.J., Liu, Z., Najmaei, S., Ajayan, P.M. & Lou, J. Large-area vapor-phase growth and characterization of MoS₂ atomic layers on a SiO₂ substrate. *Small* **8**, 966-971 (2012).
17. Mak, K.F., He, K.L., Shan, J. & Heinz, T.F. Control of valley polarization in monolayer MoS₂ by optical helicity. *Nature Nanotech.* **7**, 494-498 (2012).
18. Zeng, H.L., Dai, J.F., Yao, W., Xiao, D. & Cui, X.D. Valley polarization in MoS₂ monolayers by optical pumping. *Nature Nanotech.* **7**, 490-493 (2012).
19. Zhou, W. et al. Intrinsic structural defects in monolayer molybdenum disulfide. *Nano Lett.* **13**, 2615-2622 (2013).
20. Qiu, H. et al. Hopping transport through defect-induced localized states in molybdenum disulphide. *Nature Commun.* **4**, 2642 (2013).

21. Chen, X. et al. Electron-electron interactions in monolayer graphene quantum capacitors. *Nano Res.* **6**, 619-626 (2013).
22. Yu, G.L. et al. Interaction phenomena in graphene seen through quantum capacitance. *Proc. Nati. Acad. Sci. USA* **110**, 3282-3286 (2013).
23. Hunt, B. et al. Massive dirac fermions and Hofstadter butterfly in a van der Waals heterostructure. *Science* **340**, 1427-1430 (2013).
24. Wang, L. et al. Negative quantum capacitance induced by midgap states in single-layer graphene. *Sci. Rep.* **3**, 2041 (2013).
25. Chen, X.L. et al. Negative compressibility observed in graphene containing resonant impurities. *Appl. Phys. Lett.* **102**, 203103 (2013).
26. Wang, L. et al. Detection of resonant impurities in graphene by quantum capacitance measurement. *Phys. Rev. B* **89**, 075410 (2014).
27. Xia, J., Chen, F., Li, J. & Tao, N. Measurement of the quantum capacitance of graphene. *Nature Nanotech.* **4**, 505-509 (2009).
28. He, S. & Xie, X.C. New liquid phase and metal-insulator transition in Si MOSFETs. *Phys. Rev. Lett.* **80**, 3324-3327 (1998).
29. Zhang, Z.Q. & Sheng, P. Quantum-percolation model of electronic transport in 2-dimensional granular metal-films. *Phys. Rev. B* **44**, 3304-3315 (1991).
30. Meir, Y. Percolation-type description of the metal-insulator transition in two dimensions. *Phys. Rev. Lett.* **83**, 3506-3509 (1999).
31. Das Sarma, S. et al. Two-dimensional metal-insulator transition as a percolation transition in a high-mobility electron system. *Phys. Rev. Lett.* **94**, 136401 (2005).

32. Manfra, M.J. et al. Transport and percolation in a low-density high-mobility two-dimensional hole system. *Phys. Rev. Lett.* **99**, 236402 (2007).
33. Adam, S., Cho, S., Fuhrer, M.S. & Das Sarma, S. Density inhomogeneity driven percolation metal-insulator transition and dimensional crossover in graphene nanoribbons. *Phys. Rev. Lett.* **101**, 046404 (2008).
34. Shashkin, A. et al. Percolation metal-insulator transitions in the two-dimensional electron system of AlGaAs/GaAs heterostructures. *Phys. Rev. Lett.* **73**, 3141-3144 (1994).
35. Das Sarma, S. & Hwang, E.H. Charged impurity-scattering-limited low-temperature resistivity of low-density silicon inversion layers. *Phys. Rev. Lett.* **83**, 164-167 (1999).
36. Zomer, P.J., Dash, S.P., Tombros, N. & van Wees, B.J. A transfer technique for high mobility graphene devices on commercially available hexagonal boron nitride. *Appl. Phys. Lett.* **99**, 232104 (2011).
37. Dean, C.R. et al. Boron nitride substrates for high-quality graphene electronics. *Nature Nanotech.* **5**, 722-726 (2010).
38. Cheiwchanchamnangij, T. & Lambrecht, W.R.L. Quasiparticle band structure calculation of monolayer, bilayer, and bulk MoS₂. *Phys. Rev. B* **85**, 205302 (2012).
39. Molina-Sanchez, A. & Wirtz, L. Phonons in single-layer and few-layer MoS₂ and WS₂. *Phys. Rev. B* **84**, 155413 (2011).
40. Min, S.W. et al. Nanosheet thickness-modulated MoS₂ dielectric property evidenced by field-effect transistor performance. *Nanoscale* **5**, 548-551 (2013).
41. Lee, C. et al. Anomalous lattice vibrations of single- and few-Layer MoS₂. *ACS Nano* **4**, 2695-2700 (2010).

42. Kam, K.K. & Parkinson, B.A. Detailed photocurrent spectroscopy of the semiconducting group VIB transition metal dichalcogenides. *J. Phys. Chem.* **86**, 463-467 (1982).

Figures:

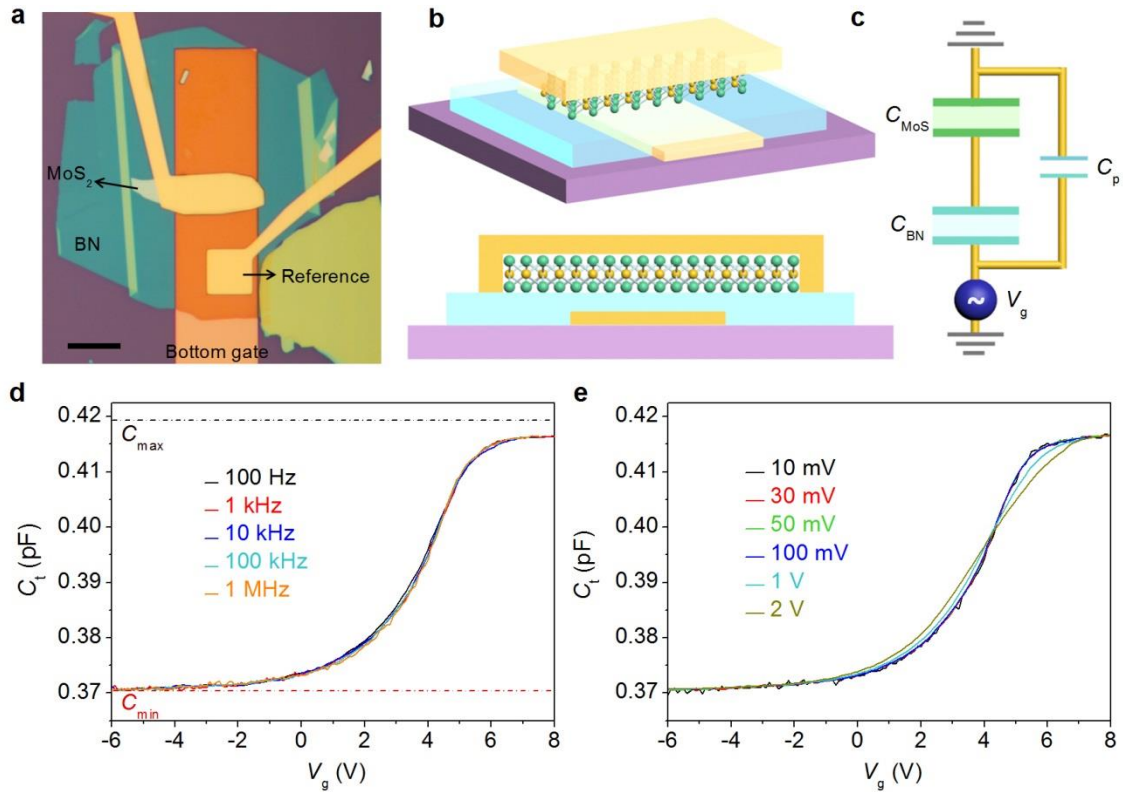


Figure 1 | The optical and schematic images of the MoS₂ MIS-M heterostructures. a,b, The MoS₂ flakes are fully covered by a top Ti/Au electrode. The square top electrode in (a) is the reference capacitor. Scale bar is 10 μ m. **c,** The equivalent circuit of the MoS₂ capacitance devices. **d,e,** Total capacitance C_t measured from a 5.9 nm-thick MoS₂ at 2 K at different frequencies (d) and excitation voltages (e) respectively. The measured capacitance in vertical heterostructures is almost independent of excitation frequencies, which differs greatly from that obtained in conventional FET structures (Supplementary Material). The excitation voltage used for (d) is 50 mV, and the frequency used for (e) is 100 kHz.

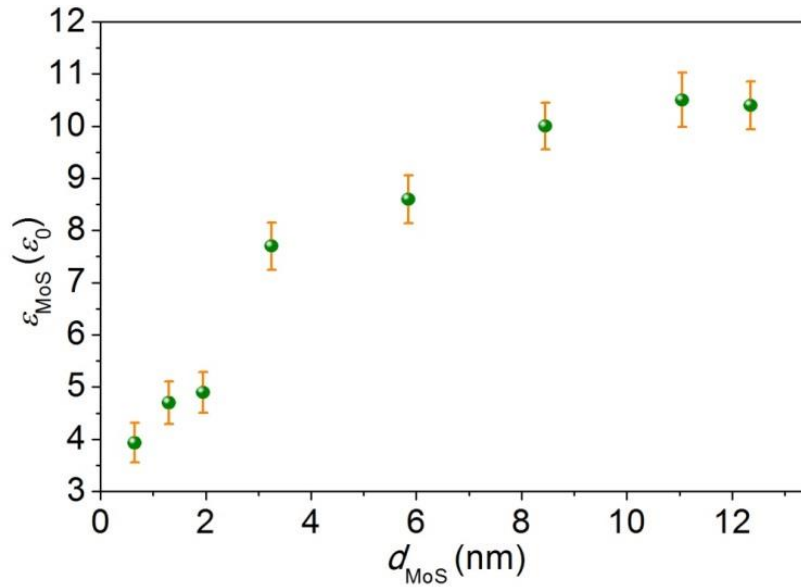


Figure 2 | Experimental data of the thickness-dependent dielectric constant of MoS₂. The dielectric constant of MoS₂ ϵ_{MoS_2} is plotted as a function of thickness d_{MoS_2} . ϵ_{MoS_2} increases from $3.9 \epsilon_0$ for a monolayer to $10.5 \epsilon_0$ for bulk MoS₂. The errors originate from the measurements of sample sizes, thicknesses of MoS₂ and BN, and capacitances of MoS₂.

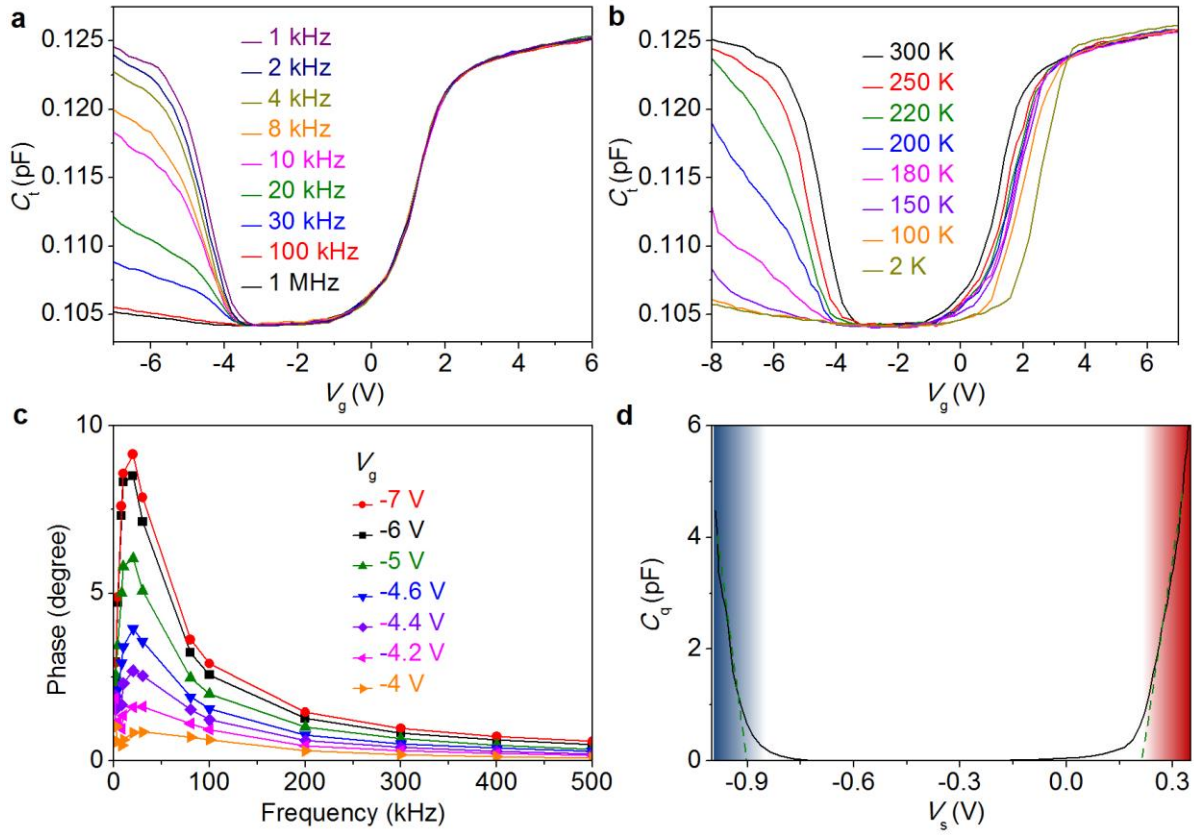


Figure 3 | The valence band of multilayer MoS₂ accessed by capacitance measurement. a, C_t measured at 300 K for different excitation frequencies. **b,** C_t measured at 1 kHz for different temperatures. **c,** Phase information plotted as a function of excitation frequencies at 300 K for different V_g . The phase peak around 20 kHz yields a relaxation time of hole carriers at 50 μ S. **d,** The quantum capacitance C_q of MoS₂ plotted as a function of surface potential V_s at 300 K, which yields a band gap width of around 1.14 eV. The excitation voltage used is 100 mV.

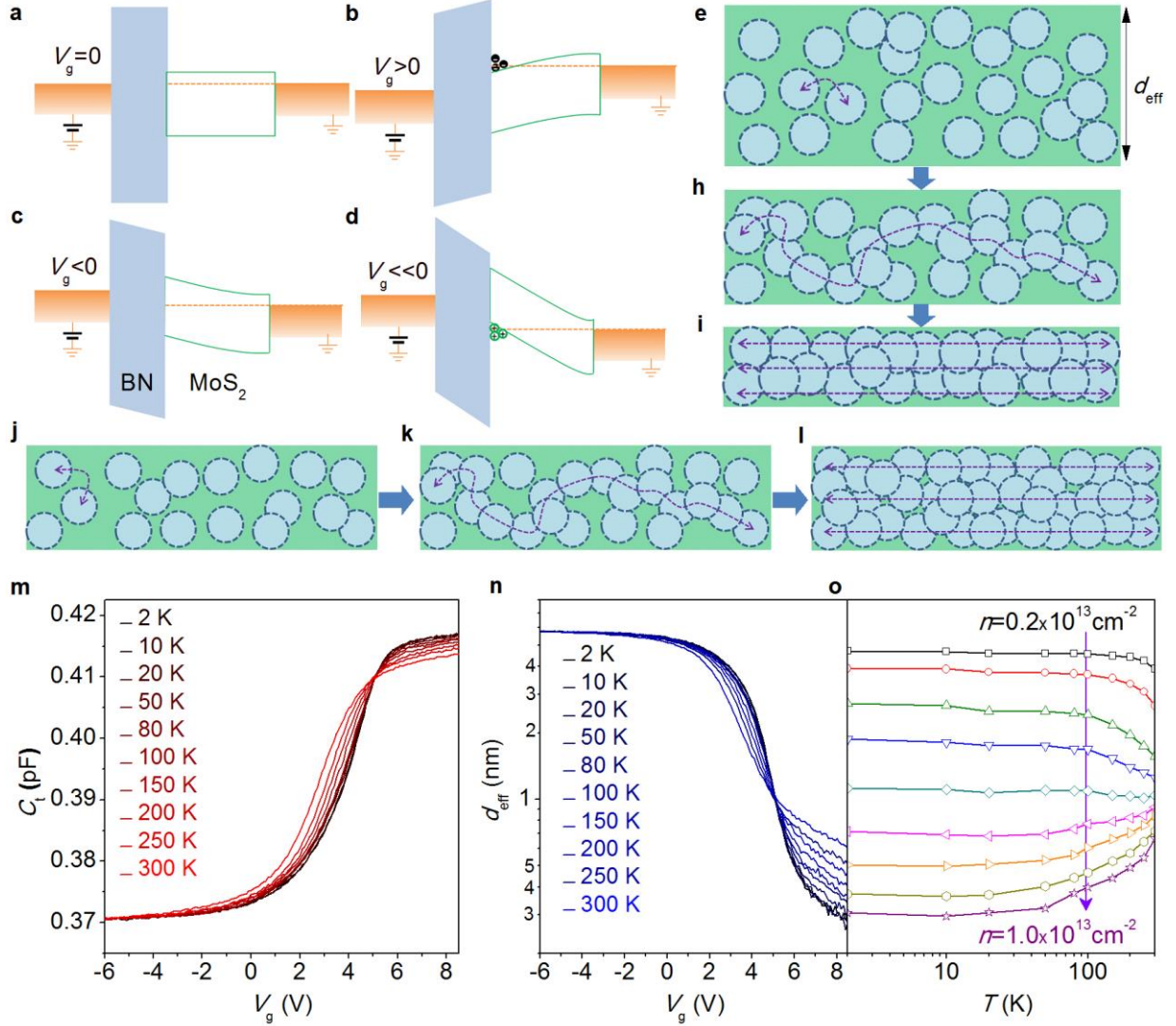


Figure 4 | The percolation transition driven by density inhomogeneity in multilayer MoS₂.

a-d, The schematic band diagrams of metal-BN-MoS₂-metal structures at flat band (**a**), accumulation region (**b**), depletion region (**c**) and inversion region (**d**). **e-l**, The schematic images showing the percolation-induced MIT under different effective thicknesses of electron states (**e-i**) and carrier densities (**j-l**). The circles denote isolated carrier puddles in MoS₂. **m,n**, The measured total capacitance C_i (**m**) and effective thickness d_{eff} (**n**) plotted as a function of gate voltage V_g for 2 K to 300 K. The excitation voltage and frequency used are 50 mV and 100 kHz respectively. **o**, d_{eff} plotted as a function of temperatures at different carrier densities n .

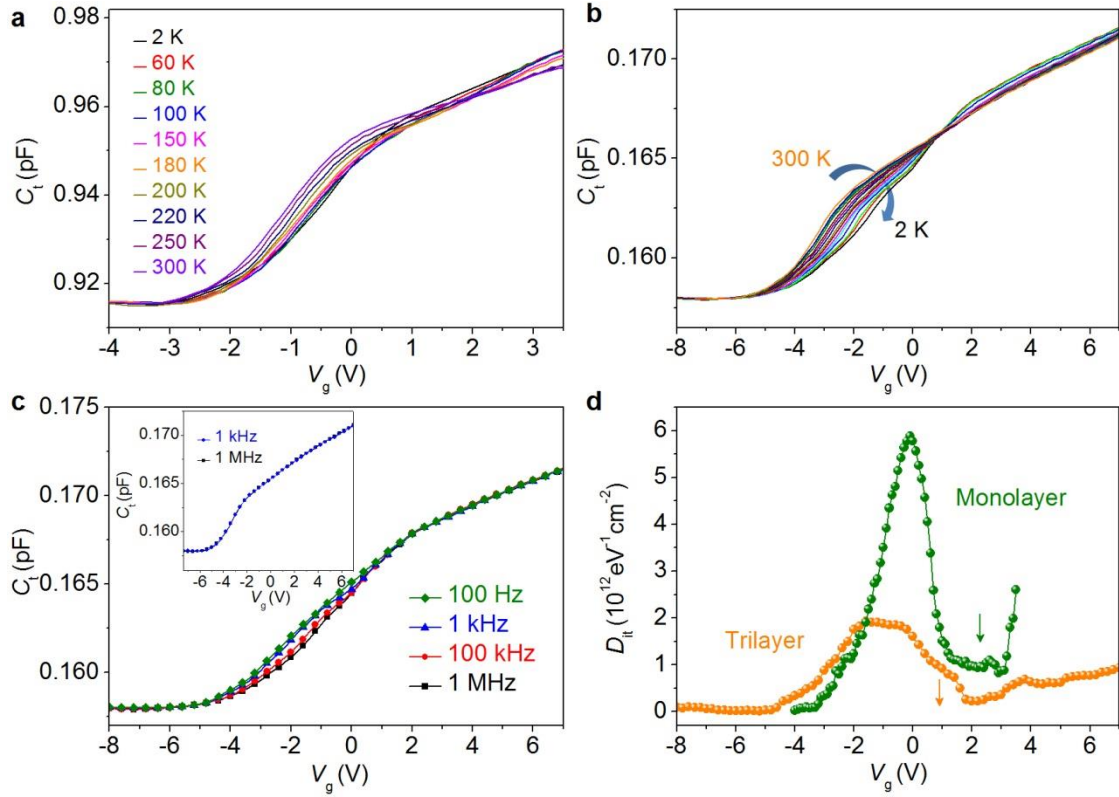


Figure 5 | The percolation transition and charge traps in monolayer and trilayer MoS₂. **a**, C_t of a monolayer MoS₂ measured at an excitation frequency 1 kHz and excitation voltage 50 mV for different temperatures. **b**, C_t of a trilayer MoS₂ measured at an excitation frequency 100 kHz. **c**, C_t of a trilayer MoS₂ measured for different excitation frequencies at 2 K, indicating that the charge traps are excited at low frequencies. The inset shows C_t measured at 300 K. **d**, The charge trap densities D_{it} as a function of V_g calculated for the monolayer and trilayer MoS₂ samples. The arrows denote the transition points.

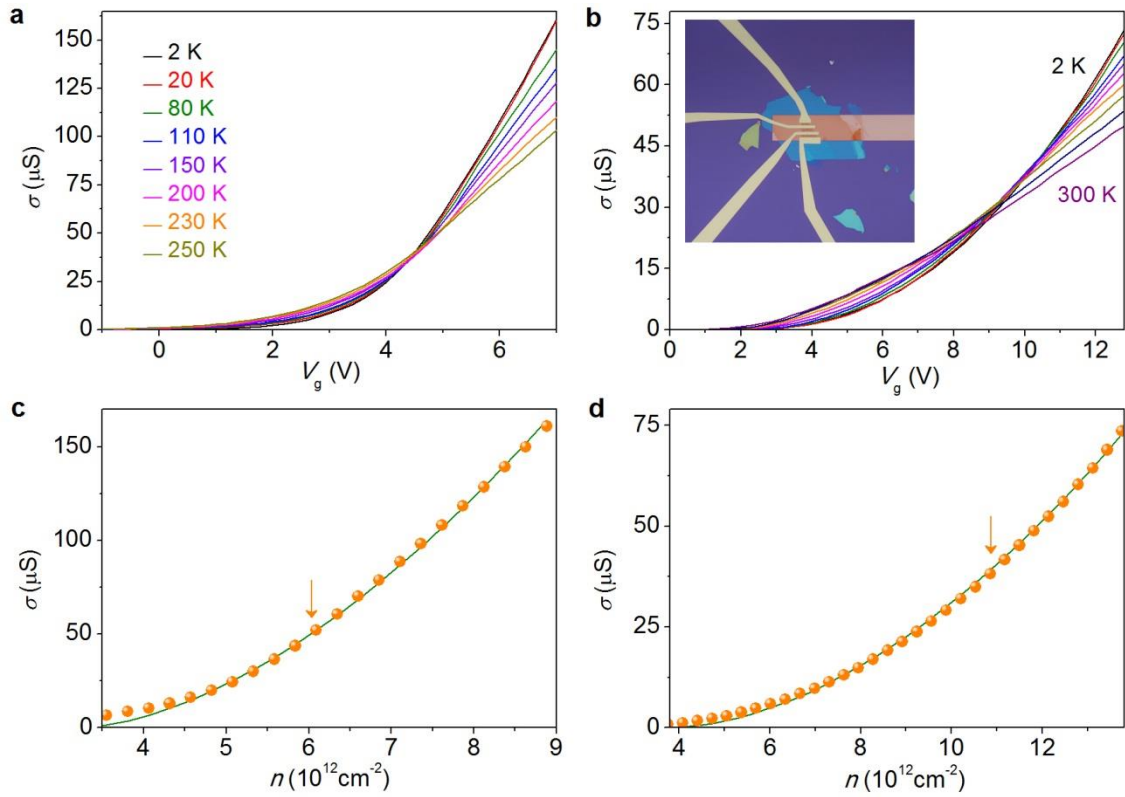


Figure 6 | Transport results showing the percolation transition in multilayer and monolayer MoS₂. **a,b**, The MITs are clearly shown by σ measurements of a multilayer (**a**) and monolayer (**b**) MoS₂ for different temperatures. The inset in (**b**) shows the optical image of a monolayer MoS₂ device. **c,d**, The fitting of experimental σ (orange dots) of multilayer (**c**) and monolayer (**d**) MoS₂ according to the percolation conductivity $\sigma=A(n-n_c)^\delta$ (green lines). The arrows denote the positions of MITs.

Supplementary Information

for

Probing the Electron States and Metal-Insulator Transition

Mechanisms in Atomically Thin MoS₂ Based on Vertical

Heterostructures

Xiaolong Chen¹, Zefei Wu¹, Shuigang Xu¹, Lin Wang², Rui Huang^{1,3}, Yu Han¹, Weiguang Ye¹,
Wei Xiong¹, Tianyi Han¹, Gen Long¹, Yang Wang¹, Yuheng He¹, Yuan Cai¹, Ping Sheng¹, Ning
Wang^{1*}

¹*Department of Physics and the William Mong Institute of Nano Science and Technology, the
Hong Kong University of Science and Technology, Clear Water Bay, Hong Kong, China*

²*Department of Condensed Matter Physics, Group of Applied Physics, University of Geneva, 24
Quai Ernest Ansermet, CH1211 Geneva, Switzerland*

³*Department of Physics and Electronic Engineering, Hanshan Normal University, Chaozhou,
Guangdong, 521041, China*

*Correspondence should be addressed to: Ning Wang, phwang@ust.hk

Capacitance measurements on MoS₂-based FET structures

Based on standard field-effect transistor (FET) structures, the top electrode is partially covered on MoS₂ as shown in Fig. S1a-c (a monolayer MoS₂ sample). S_{\max} represents the overlapping area between the bottom gate and MoS₂, and S_{\min} represents the overlapping area between the top electrode and bottom gate. In the partially-covered top electrode structure, $S_{\min} < S_{\max}$. Fig.

S1d-g show the capacitance results from a monolayer MoS₂ sample partially covered by a Ti/Au electrode. Under negative bias, MoS₂ is in the depleted state, and the measured capacitance can

be described by $C_{\min} = S_{\min} \cdot \left(\frac{d_{BN}}{\epsilon_{BN}} + \frac{d_{MoS}}{\epsilon_{MoS}} \right)^{-1}$. With increasing the gate voltage, electrons start to

accumulate at the surface of MoS₂ and the channel becomes conductive. Then, the measured

capacitance approaches $C_{\max} = S_{\max} \cdot \frac{\epsilon_{BN}}{d_{BN}}$. The ratio of C_{\max} and C_{\min} for this sample is

$C_{\max} / C_{\min} \approx S_{\max} / S_{\min} = 2.2$. This is because the term $\frac{\epsilon_{MoS}}{d_{MoS}}$ only contributes about one twentieth

of the capacitance C_{\min} , which is negligible in comparison to the capacitance increase caused by

the increase of conducting area (from S_{\min} to S_{\max}) of MoS₂.

The capacitance measured from the partially-covered MoS₂ devices largely depends on temperatures and frequencies as shown in Fig. S1d-g. The capacitance increases with decreasing excitation frequencies. This is consistent with previously reported results measured at 300 K¹.

The frequency-dependent behavior of the partially-covered devices becomes serious at low temperatures (Fig. S1f). At low temperatures and higher frequencies, MoS₂ sheets are normally not fully charged. This is attributed to the charge trapping effect or the huge lateral resistance of MoS₂ near the band edge. Hence, some intrinsic characteristics of MoS₂ are smeared, especially at low temperatures.

Extracting the parallel capacitance C_p

To accurately determine the charge trap densities, dielectric constant and quantum capacitance of MoS₂, the parallel capacitance C_p shown in Fig. 1c has to be determined first. C_p contains two terms: the residual capacitance C_r originating from the measurement setup (the measurement of C_r will be introduced in next section which is negligible compared to C_{ex}) and the parallel capacitance C_{ex} originating from the extra area of the top electrode, as shown in Fig. S2.

S_t is the total effective capacitance area enclosed by the purple dash-dot line. S_{MoS} is the effective area of MoS₂ enclosed by the red dashed line. The extra area of top electrode is $S_{ex} = S_t - S_{MoS}$. The actual capacitance $C_t' = C_t + C_{ex} + C_r$, where C_t is the capacitance shown in the main text which excludes the extra capacitance $C_{ex} = S_{ex} \cdot \frac{\epsilon_{BN}}{d_{BN}}$ and C_r . Then capacitance C_t equals to $C_t = (C_{MoS}^{-1} + C_{BN}^{-1})^{-1}$ which corresponds to area S_{MoS} .

To determine C_{ex} , we only need to know the capacitance of BN per unit area, which can be simply obtained through measuring the reference capacitor shown in Fig. 1a in the main text. We have measured the thicknesses of MoS₂ and BN sheets by atomic force microscopy (AFM) in order to determine the dielectric constant of MoS₂ (Fig. S3). The thickness of BN is 14 nm for 5.9 nm-MoS₂ device, 6.0 nm for monolayer-MoS₂ device, 14.9 nm for trilayer-MoS₂ device, and 13.5 nm for 12 nm-MoS₂ device as shown in the main text. The extracted dielectric constant of BN is around 3.1, consistent with previous results².

Determining the residual capacitance C_r

The residual capacitance C_r is accurately determined by a simple method shown in Fig. S4. In the device structure without any overlap between the top electrode and bottom gate (Fig. S4a), there is a non-conductive channel in MoS₂ which cannot be tuned by the bottom gate. Charges from electrodes are blocked from reaching the MoS₂ area above the bottom gate. Then, the measured capacitance should be the residual capacitance C_r induced by the measurement setup. The optical image of the 5.9 nm-MoS₂ sample before covering the top electrode is shown in Fig. S4b. The measured capacitance along with a 3.3 nm-MoS₂ sample is plotted in Fig. S4c. We find that the capacitance values of C_r are in the order of ~fF, which is about 3-order smaller than the MoS₂ capacitances. Hence, the residual capacitance C_r is ignored in our calculations.

Capacitance measurements on the MoS₂ device with Cr/Au top electrodes.

The work function of Cr (~4.5 eV) is larger than that of Ti (~4.3eV). Hence, Cr is much closer to the valence band of MoS₂, and a smaller relaxation time of holes should be observed. In the MoS₂ sample coated with a Cr/Au electrode (Fig. S5a), the formation of the inversion layer is observed at 2 K where the contribution of thermal effects can be neglected. As confirmed by the capacitance results measured at different excitation voltages (Fig. S5b), leakage current (to the electrode contacts) plays an important role. Large excitation voltages can contribute significantly to the formation of holes. As the work function of Cr is about 0.2 eV higher than the electron affinity of MoS₂ (~4.3 eV), the relaxation of electrons is also subjected to the Schottky barrier (Fig. S5a,b) which shows frequency- and temperature-dependent behavior in capacitance measurements. At 300 K, the relaxation time of holes is much shorter (~5 μ s) than that at low

temperatures, while the capacitance measured at the electron side is almost frequency-independent.

Modeling capacitance devices and extracting the quantum capacitance C_q of thin MoS₂ flakes

Here, we applied the Poisson equation to investigate our capacitance devices quasi-quantitatively and consider a simplified one-dimensional model³ as shown in Fig. S6a and b:

$$\frac{d^2V}{dx^2} = -\frac{e(n_D^+ - n - p_A^- + p)}{\epsilon_{MoS}} \quad (1)$$

where V is the potential of MoS₂ at position x . n_D^+ and p_A^- are the densities of electron and hole donors respectively. n and p represent the electron and hole carrier densities. Assuming n_0 and p_0 are the equilibrium densities of electrons and holes respectively (at $V = 0$), we have $n = n_0 \exp(\frac{eV}{kT})$ and $p = p_0 \exp(-\frac{eV}{kT})$, where k is the Boltzmann constant. When $V = 0$, the charge neutrality condition applies, and we have $n_D^+ - p_A^- = n_0 - p_0$. Here, we only focus on the depletion and accumulation regions of MoS₂ devices where $n_0 \gg p_0$. Then the Poisson equation can be simplified as:

$$\frac{d^2V}{dx^2} = \frac{en_0}{\epsilon_{MoS}} [\exp(\frac{eV}{kT}) - 1] \quad (2)$$

As the electric field in MoS₂ is described by $E = -\frac{dV}{dx}$, the integral of Eq. (2) yields:

$$E = \sqrt{E_0^2 + \frac{2k^2T^2}{e^2L_D^2} [\exp(\frac{eV}{kT}) - \frac{eV}{kT} - 1]} \quad (3)$$

where $L_D = \sqrt{\frac{\epsilon_{MoS} kT}{e^2 n_0}}$ is the Debye length. E_0 is the electric field at position $x = d_{MoS}$ (the interface between MoS₂ and top electrode shown in Fig. S6a,b). E_0 is a non-zero value and mainly determined by the gate voltage V_g because of the finite thickness of MoS₂. E_0 can be obtained through the constraint condition $\int_0^{V_s} \frac{dV}{E} = d_{MoS}$, where V_s is the surface potential of MoS₂. As a result, any additional charges $Q_s' = \epsilon_{MoS} E_0$ will be accumulated at the interface between the top electrode and MoS₂ (Fig. S6a,b). The total charges induced in the device can be described by $Q_t = \epsilon_{MoS} E_s = Q_{MoS} + Q_s'$, where E_s is the surface electric field of MoS₂, and Q_{MoS} is the surface charges in MoS₂.

The simulating parameters for Fig. S6, S7, and S8 are: $\epsilon_{MoS} = 8.6$, $d_{MoS} = 5.9\text{nm}$, $\epsilon_{BN} = 3$, $d_{BN} = 13.5\text{nm}$ and doping density $n_D^+ = 10^{17}\text{cm}^{-2}$. The simulated total capacitance $C_t = \frac{dQ_t}{dV_g}$ as a function of V_g is shown in Fig. S6c. Compared to C_t of MoS₂ with an infinite thickness, C_t with a finite value of d_{MoS} approaches a constant value $(\frac{d_{MoS}}{\epsilon_{MoS}} + \frac{d_{BN}}{\epsilon_{BN}})^{-1}$ in the depletion region, consistent with the experimental observations shown in the main text. The simulations for charge and potential distributions in MoS₂ are shown in Fig. S7. In the accumulation region, most of charges are distributed in the first several layers of MoS₂. While in the depletion region, the charge density is small (mainly originated from the density of electron donors n_D^+). As a result, the charge distribution is almost constant in MoS₂. This analysis also supports that the effective thickness d_{eff} decreases with increasing the gate voltage.

The capacitance of MoS₂ $C_{MoS} = \frac{dQ_t}{dV_s}$ can be written as $C_{MoS} = C_q + C_s'$, where $C_q = \frac{dQ_{MoS}}{dV_s}$ is the quantum capacitance of MoS₂ and $C_s' = \frac{dQ_s'}{dV_s}$ originates from the charges induced at the interface between the top electrode and MoS₂. C_{MoS} can be obtained from the serial connection relationship $C_t = (C_{MoS}^{-1} + C_{BN}^{-1})^{-1}$. However, it is difficult to directly determine C_s' as discussed below.

Here, we present an approximate method to satisfactorily extract the quantum capacitance (C_q) of MoS₂, supported by theoretical calculations. The accurate C_{MoS} , C_s' and C_{q-th} , without adopting any approximation, are theoretically simulated and shown in Fig. S8. In the depletion region, both C_s' and C_{MoS} approaches a constant value C_{s0} . With increasing the gate voltage, C_s' decreases due to the stronger screening effect of accumulated charges at the surface of MoS₂. While, C_{q-th} increases rapidly. The quantum capacitance of MoS₂ can be approximately written in the form of $C_{q-ex} = C_{MoS} - C_{s0}$ instead of $C_{q-th} = C_{MoS} - C_s'$ with a good accuracy as shown in Fig. S8. In the depletion region, all charges form at the interface between the top electrode and MoS₂. Then, we have $C_{MoS} = C_s'$, and $C_{q-th} = C_{q-ex} = 0$. The approximation is accurate in the depletion region. In the accumulation region, $C_s' < C_{s0}$ and there exists deviation between the approximation value C_{q-ex} and the accurate value C_{q-th} . In this case, surface charges dominate the total induced charges in the device and thus $C_{q-th} \gg C_s'$. Obviously, the deviation is small compared to the value of C_{q-th} . Overall, $C_{q-ex} = C_{MoS} - C_{s0}$ is a good approximation to the accurate value of C_{q-th} .

References

1. Zhu, W. J. *et al.* Electronic transport and device prospects of monolayer molybdenum disulphide grown by chemical vapour deposition. *Nature Commun.* **5**, 3087 (2014).
2. Dean, C. R. *et al.* Boron nitride substrates for high-quality graphene electronics. *Nature Nanotech.* **5**, 722-726 (2010).
3. Kingston, R. H. & Neustadter, S. F. Calculation of the space charge, electric field, and free carrier concentration at the surface of a semiconductor. *J. Appl. Phys.* **26**, 718 (1955).

Figures

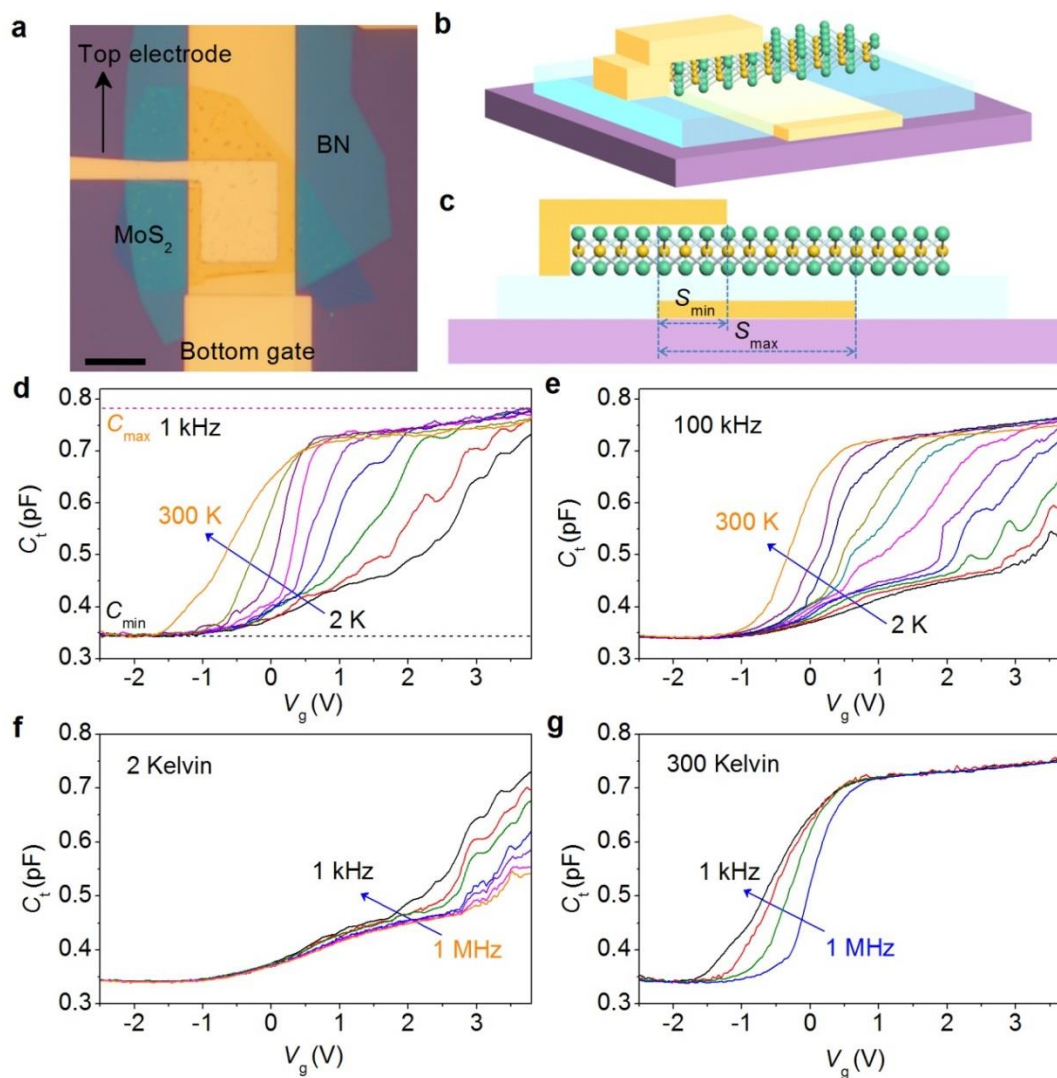


Fig. S1 | Capacitance characteristics for a monolayer MoS₂ in MIS-FET geometry. a-c, Optical (a) and schematic images (b,c) of the partially-covered top electrode geometry for capacitance measurements. Scale bar is 10 μm . d,e, C_t at excitation frequency 1 kHz (d) and 100 kHz (e) for different temperatures. f,g, C_t at temperature 2 K (f) and 300 K (g) for different excitation frequencies.

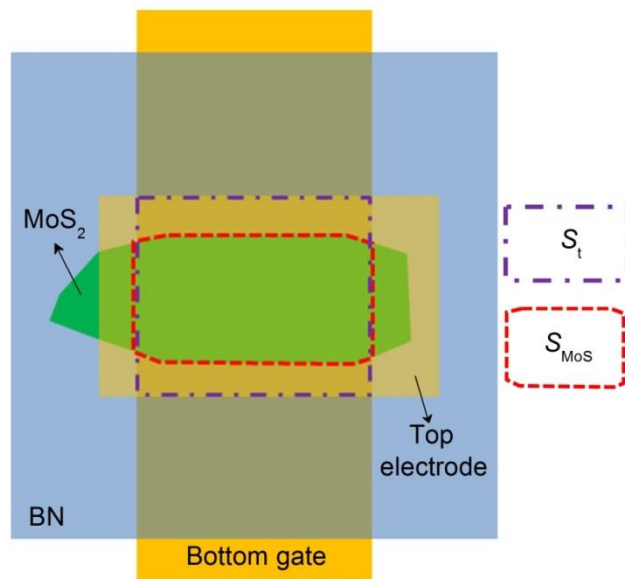


Fig. S2 | Analysis of the device geometry. S_t is the total effective capacitance area enclosed by the purple dash-dot line. S_{MoS} is the effective area of MoS₂ enclosed by the red dashed line.

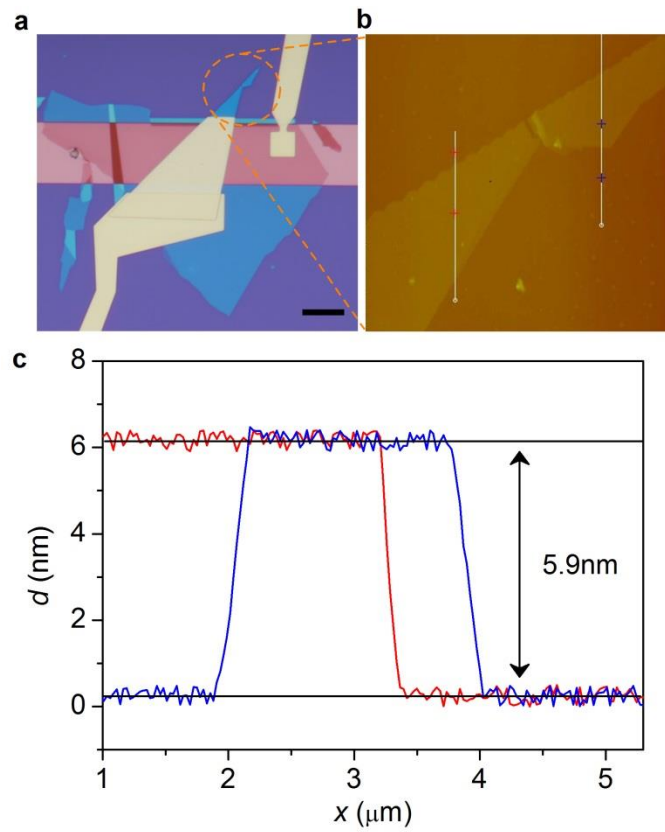


Fig. S3 | Determination of the thickness of MoS₂ by AFM. **a**, Optical image of the 5.9nm-thick MoS₂ sample shown in the main text. **b,c**, AFM image (**b**) and the thickness (**c**) of the MoS₂ sample.

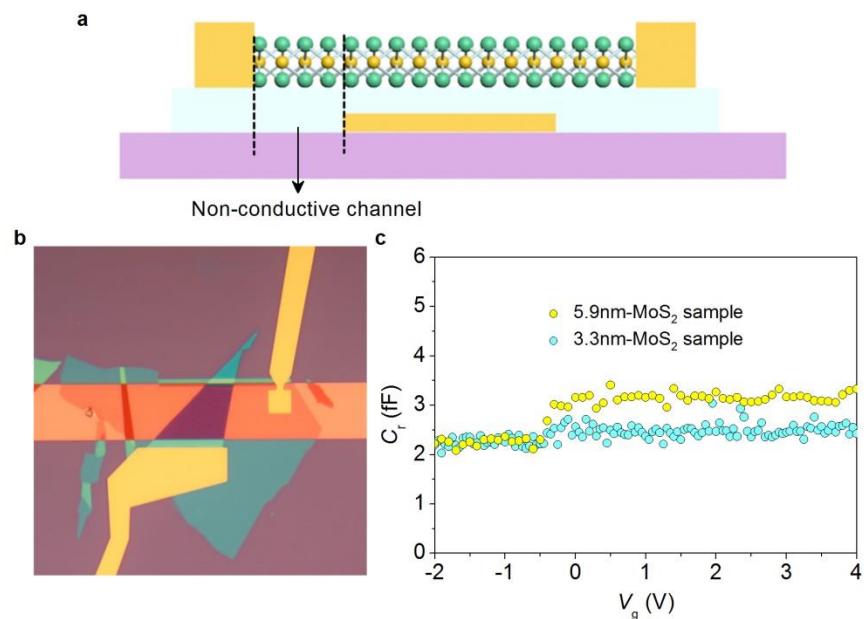


Fig. S4 | Determination of the residual capacitance C_r . **a**, Schematic image of the MoS₂ sample without overlapping between the top electrode and bottom gate. **b**, Optical image of the 5.9 nm-MoS₂ sample before covering the top electrode. **c**, Residual capacitance determined in the 5.9 nm-MoS₂ sample along with a 3.3 nm-MoS₂ sample. It is three-order smaller than the capacitance of MoS₂ devices.

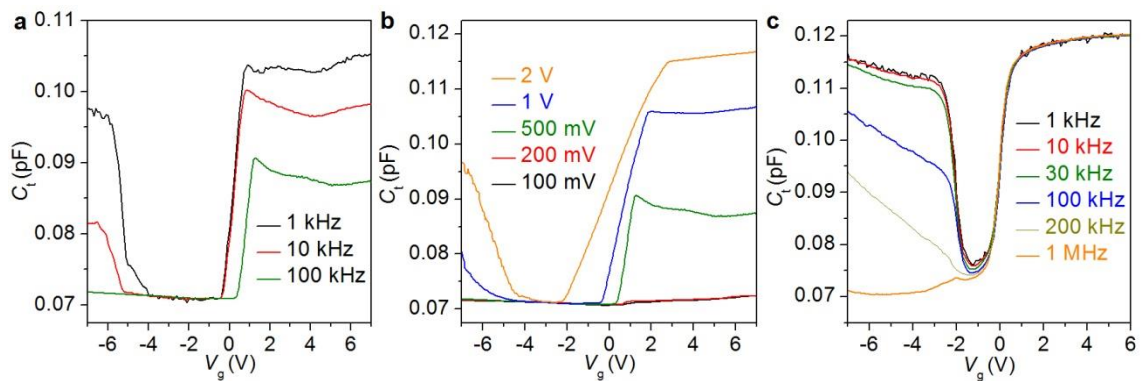


Fig. S5 | MoS₂ capacitance with Cr/Au electrodes. **a**, Measured capacitance C_t at 2 K with an excitation voltage 500 mV for different frequencies. **b**, C_t at 2K with an excitation frequency 100 kHz at different excitation voltages. **c**, C_t at 300 K with an excitation voltage 200 mV for different frequencies.

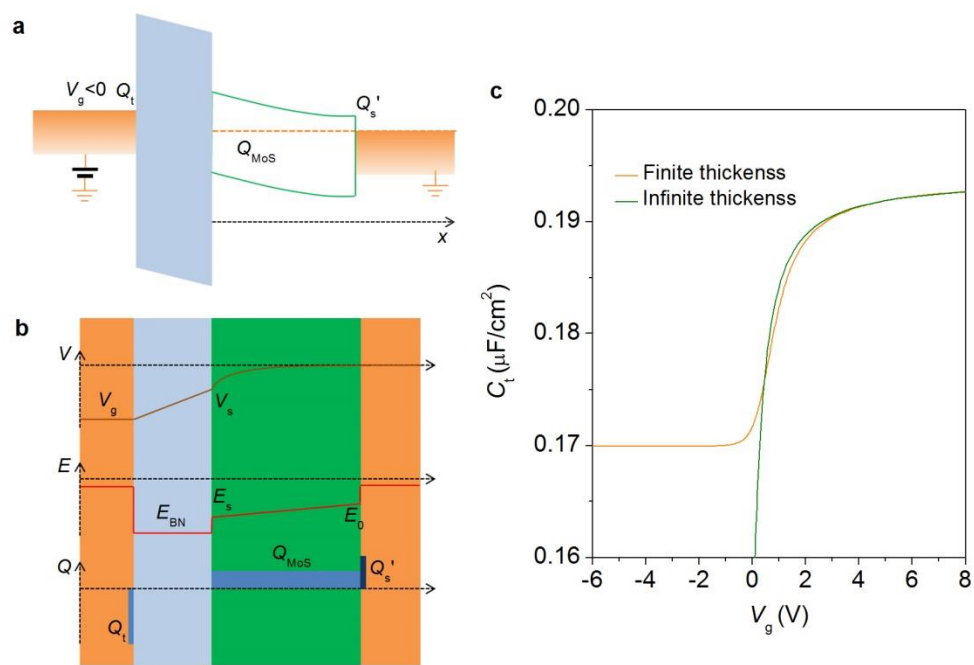


Fig. S6 | Modeling of capacitance devices. **a**, Schematic band diagram at the depletion region. **b**, Schematic image of potentials, electric fields, and charge distributions in the capacitance device. **c**, Simulated total capacitance C_t as a function of gate voltage V_g with a finite thickness $d_{\text{eff}} = 5.9\text{nm}$ (orange line) and an infinite thickness (green line).

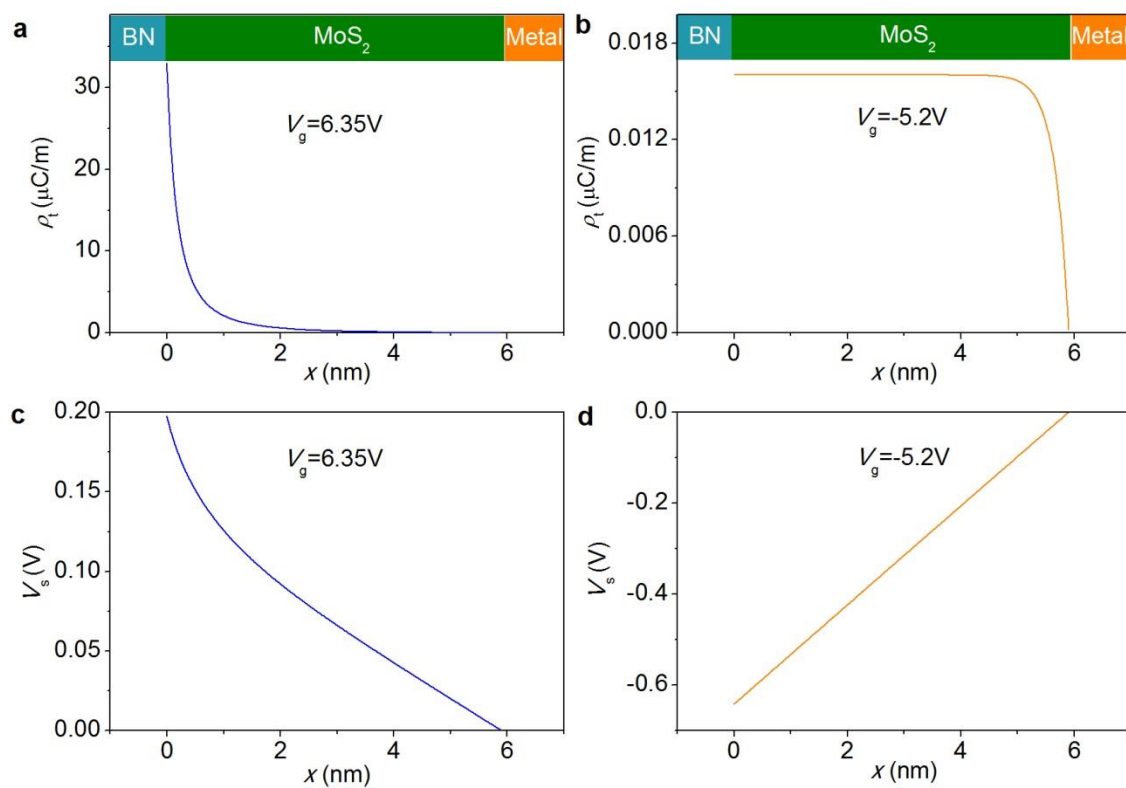


Fig. S7 | Charge and potential distributions in MoS₂. **a,c**, Charge (**a**) and potential (**c**) distributions in the accumulation region with a gate voltage $V_g = 6.35\text{V}$ in the MoS₂ capacitance device. **b,d**, Charge (**b**) and potential (**d**) distributions in the depletion region with a gate voltage $V_g = -5.2\text{V}$.

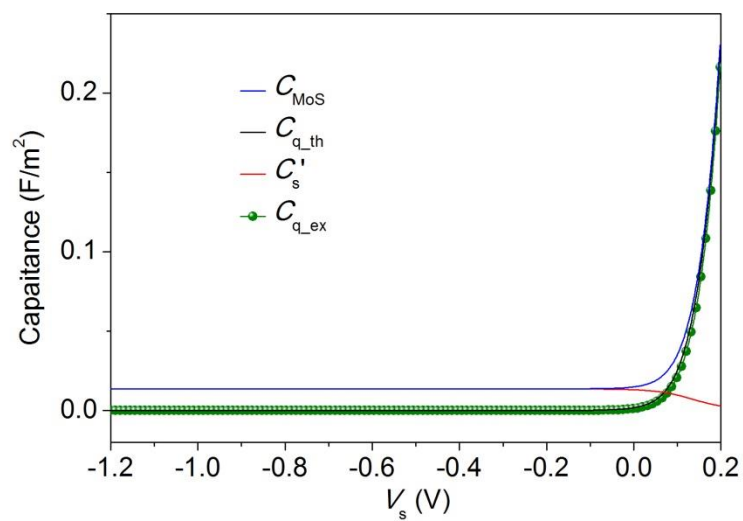


Fig. S8 | Extraction of the quantum capacitance of MoS₂. Simulated results of C_{MoS} , C_s' and C_{q_th} without adopting any approximation. C_{q_ex} is a good approximation of C_{q_th} .